FP7-SPACE-2011-1
Grant Agreement Number 284520

MAARBLE
Monitoring, Analyzing and Assessing Radiation Belt Loss and Energization

Final Report

Grant Agreement number: 284520
Project acronym: MAARBLE
Project title: Monitoring, Analyzing and Assessing Radiation Belt Loss and Energization
Funding scheme: FP7-CP
Period covered: January 2012 - December 2014
Editor: Ioannis A. Daglis (iadaglis@phys.uoa.gr)
Project website address: http://www.maarble.eu

1. Executive summary

The MAARBLE project had two focused and synergistic aims:

i. to advance scientific research on radiation belt dynamics, in particular during periods of enhanced geomagnetic activity when the most dramatic changes occur;

ii. to enhance data exploitation of European space missions through the combined use of European and United States spacecraft measurements and ground-based observations.

MAARBLE employed multi-spacecraft monitoring of the geospace environment, complemented by ground-based monitoring, in order to analyse and assess the physical mechanisms leading to radiation belt particle energization and loss. These processes are of great importance, because radiation enhancements due to radiation belt energization can adversely impact satellites that modern society increasingly depends on.

MAARBLE paid particular attention to the properties of ultra-low frequency (ULF) and very low frequency (VLF) waves and their critical role in radiation belt dynamics. As a central deliverable, a database containing characteristic properties of ULF and VLF waves was created and is now publicly available to the scientific community. Based on the wave database, statistical models of wave activity for different types of waves were created. These models - or maps - provide statistical distribution of amplitudes and, moreover, wave normal angles and other polarization and propagation characteristics, which determine how the waves interact with particles.

Another central task of MAARBLE was to use data assimilation techniques to guide 'the best' estimate of the state of a complex system such as the electron radiation belt. Multi-spacecraft particle measurements were incorporated into the ONERA data assimilation tool, which is in essence an ensemble Kalman filter. Next, the performance and capabilities of the data assimilation tool were enhanced. One of the major improvements regarding data assimilation itself has been to implement the capability of ingesting count rates data. The validation of the improved data assimilation tool was satisfactory and showed that with its capabilities extended and its performance significantly improved, this ensemble Kalman filter could serve as the essential means to balance model predictions with data.

One of the most significant outcomes from the MAARBLE project was new scientific discoveries and new knowledge about the conditions under which different and competing wave-particle interactions control the dynamics of the electron radiation belts – as well as new understanding of when and where specific mechanisms dominate the delicate balance between competing acceleration and loss. Using a new and unique approach to data-driven specification of radial diffusion, we discovered fundamental new impacts of inward and outwards transport, controlled by the availability of plasma-sheet source populations and/or the occurrence of magnetopause shadowing. We furthermore determined when a wide range of plasma wave-particle interactions contribute to loss or acceleration, and for the first time proved EMIC waves can cause the Van Allen belt electron loss by scattering into the atmosphere.

Overall, the MAARBLE project generated extensive new knowledge in a very large number of scientific publications in leading international scientific journals (38 papers), with many exciting and high-impact scientific publications expected to provide guidance and new research directions for the international radiation belt community for many years to come.

2. Summary description of project context and objectives:

The highly energetic particle environment of the Van Allen radiation belts in near-Earth geospace is extremely dynamic and undergoes continual changes through acceleration and loss processes. These processes are of great importance, because particle radiation enhancements can adversely impact satellites that modern society increasingly depends on.

The MAARBLE project aimed at unravelling the details of these processes that govern radiation belt dynamics - in particular during periods of enhanced geomagnetic activity when the most dramatic changes occur. It did so through effective data exploitation of European space missions in combination with exploitation of data from US spacecraft measurements and European and Canadian ground-based observations, in order to analyse and assess the physical mechanisms leading to radiation belt particle energization and loss.

Electromagnetic waves play a fundamental role in the acceleration of electrons to very high energies (typically MeV), and also the loss of electrons and ions from the radiation belts into the atmosphere. Wave-particle interactions play a major role governing the variability of the Earth's outer electron radiation belt, where the flux can vary by up to five orders of magnitude on timescales usually measured in hours to days, but which can be as short as two minutes. Wave-particle interactions refer to a resonant interaction between the waves and the particles, leading to a very efficient exchange of energy and momentum. The frequencies of the most important waves are typically of the order of the electron cyclotron frequency, which in the radiation belts may vary from about a few kHz to several hundred kHz, and of the order of the ion cyclotron frequency, which may range from less than 1 Hz to ~100 Hz. Particular attention is paid to the role of ultra low frequency (ULF) and very low frequency (VLF) waves.

A database containing properties of the ULF and VLF waves has been created and made available to the scientific community. Based on the wave database, a statistical model of the wave activity dependent on the level of geomagnetic activity, solar wind forcing, and magnetospheric region is developed.

Multi-spacecraft particle measurements have been incorporated into data assimilation tools, leading to new understanding of the causal relationships between ULF/VLF waves and radiation belt dynamics. Data assimilation techniques have been proven as a valuable tool in the field of radiation belts, able to guide 'the best' estimate of the state of a complex system.

Specifically, the objectives of the project have been:

- to use data assimilation techniques to guide 'the best' estimate of the state of a complex system such as the electron radiation belts;
- to create a database of ULF and VLF waves in the radiation belts that is complementary to other Seventh Framework Programme (FP7) projects, and which has been disseminated to the scientific community through ESA's Cluster Science Archive (CSA) website;
- to develop a statistical model of radiation belts relevant wave activity;
- to elaborate on specific aspects of wave-particle interactions, which are of strong relevance to radiation belt dynamics.

Combining a radiation belt physical model and in-situ data via a data assimilation tool has been shown to be very powerful in retrieving the global dynamic true state of the radiation belts. The analysis of the performance of the data assimilation tool clearly indicates that it is not necessary to have a large amount of data to assimilate in order to converge toward the true state. Even if one has only measurements along one GEO and one navigation (GPS) orbit, it will still be enough to drive the tool toward the true state with acceptable uncertainties.

Overall, the scientific discoveries facilitated by funding from the European Commission have validated the excellence of the European scientific community placing European researchers at the forefront of international endeavour in this high profile field. Moreover, the research results will contribute significantly to future improvements in space weather forecasting and the specification of space situational awareness, which are also at the core of current high priority actions within Europe and at the European Space Agency.

3. Description of the main S&T results of the MAARBLE project

3.1 Particle data assimilation

The objective of WP2 - one of the main objectives of the MAARBLE project - was to use data assimilation techniques to guide 'the best' estimate of the state of a complex system such as the electron radiation belts, taking advantage of a physical model for the radiation belts (global to the system but never perfect due to modelling uncertainties) to overcome some of the problems associated with the paucity of measurements arising from limited spatial and energy coverage. First, a standardized radiation belt electron database was developed. The data were collected from eight European missions, XMM/ERMD, INTEGRAL/IREM, PROBA-1/SREM, GIOVE-B/SREM and CLUSTER/RAPID – 1 to 4 and seven US missions, THEMIS/SST – A, B, C, D, E, POLAR/CEPPAD and GOES/SEM. All data sets from selected spacecraft/instrument couples were standardised into unique daily files in common Data File Format (CDF) following ISTP/PRBEM guidelines. Following those guidelines can facilitate data standardization and exchange to the users' community. The data are publicly available on a dedicated MAARBLE website: http://craterre.onecert.fr/MAARBLE/.

All individual data sets were carefully analysed in terms of data quality. One must be aware that ionising particle measurements in space are difficult to perform and is still challenging due to limited weight, power, and space available on-board spacecraft. Particular attention was paid to channel saturation, background and contamination by other species (e.g., protons instead of electrons). An in-depth analysis method was developed for the European Space Agency SREM instrument measurements and has been published in a peer-reviewed journal (Bourdarie et al., 2014). An example is given below for two distinct channels, TC3 and S34, corresponding to almost the same energies for protons but to distinct energies for electrons. When the distribution of points, acquired over years, is mapped against TC3 and S34 count rates (Figure 1) two branches can be seen:

- one dense branch below the solid red line (area 3); and
- a second branch above the dashed red line (area 5).

Nevertheless, many points can be seen between the two red lines (area 4). It should also be noted that area 1 corresponds to time when TC3 measurements are below background value and area 2 to time when S34 count rates are below background value. A vertical cut in the distribution of points mapped against TC3 and S34 count rates for S34=1.5 counts/sec is shown in Figure 2: the transition from region 3 to 4 and 4 to 5 are well seen and are indicated by vertical red lines. Particle specie can be associated to TC3 and S34 for each of these areas (Figure 3). When the time range to perform the statistics is reduced to times when the slot region is never filled by energetic electrons, we found that the lower branch (region 3) is induced by times when proton counts dominate in both channels. This is consistent with the TC3 and S34 proton response function: the slope of this branch is close to 1.

Next, if the time range to perform the statistics is reduced to times when the slot region is filled by energetic electrons, then the scattered points above the solid red line appears (region 4). This is to say TC3 measures electrons while S34 still measures trapped protons. A function can then be defined as a separator between region 3 and 4 (see solid red line in

Figure 1). In this case it is defined as $y = 10^{1 \cdot \log 10(x) + 0.95}$.

Over the time span of PROBA-1/SREM in space, two major magnetic storms were recorded: during the months July and August 2004 and in November 2004. During those events, electrons were accelerated to very high energies. Count rates acquired during those two events correspond to region 5, i.e., TC3 and S34 count rates are dominated by electrons. Finally, we found that in the outer belt and in the absence of solar flare, S34 count rates are below background while TC3 count rates can be very high, i.e. S34 is affected by cosmic rays while TC3 count rates are dominated by electrons. This corresponds to region 2. Defining separation lines between each region, it is then possible to assign to each measurement well-defined particle species. Of course, each area being defined from statistics, an uncertainty around each separation curve ($y = f(x)$) must be considered. It was set to $y*10^{0.3}$ and $y*10^{-0.3}$. In between, the species of particles was set to "undefined".

The results are shown in Figure 4, where PROBA-1/SREM TC3 count rates are plotted in an L-shell versus time map, with all count rates in bottom panel, only electrons in second panel from bottom, only protons in third panel from bottom, and unknown in top panel. While individual solar flares as well as the solar cycle modulation of the proton belt is not clearly seen in the bottom panel where all count rates are reported, it becomes more than clear in the third panel from bottom where only count rates attributed to protons are sorted. Also, a transient inner electron belt with energies greater than 500 keV is well seen in the second panel from bottom. Electron life times in the inner belt could be then extracted. They are shorter than those of trapped protons.

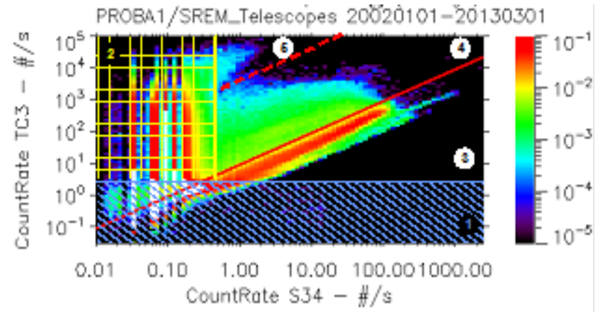

Figure 1: Distribution of points mapped against TC3 and S34 count rates. The colour bar indicates the percentage of points in a bin.

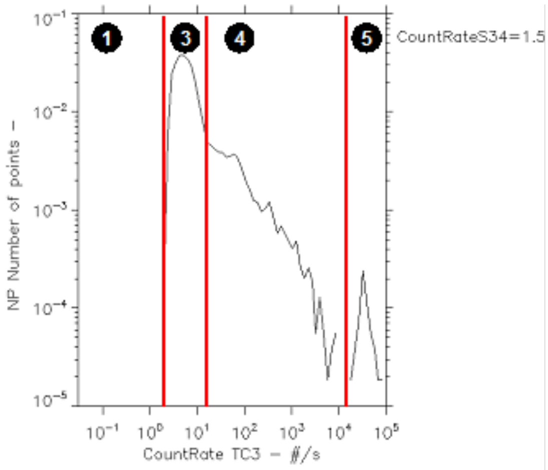

Figure 2: Vertical cut in the distribution of points mapped against TC3 and S34 count rates for S34=1.5 #/s.

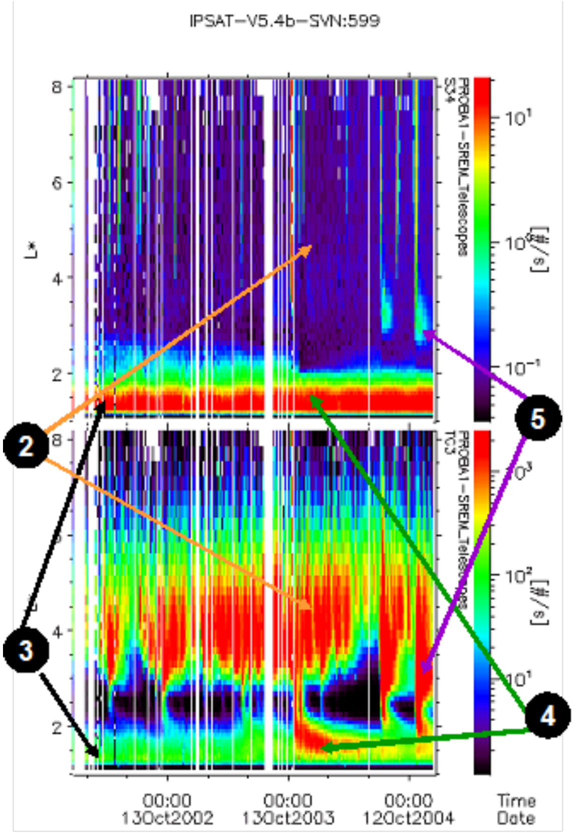

Figure 3: Overview plot in an L-shell versus time from March 1, 2002 to January 1, 2005. The top panel corresponds to the S34 channel and bottom shows the TC3 count rate.

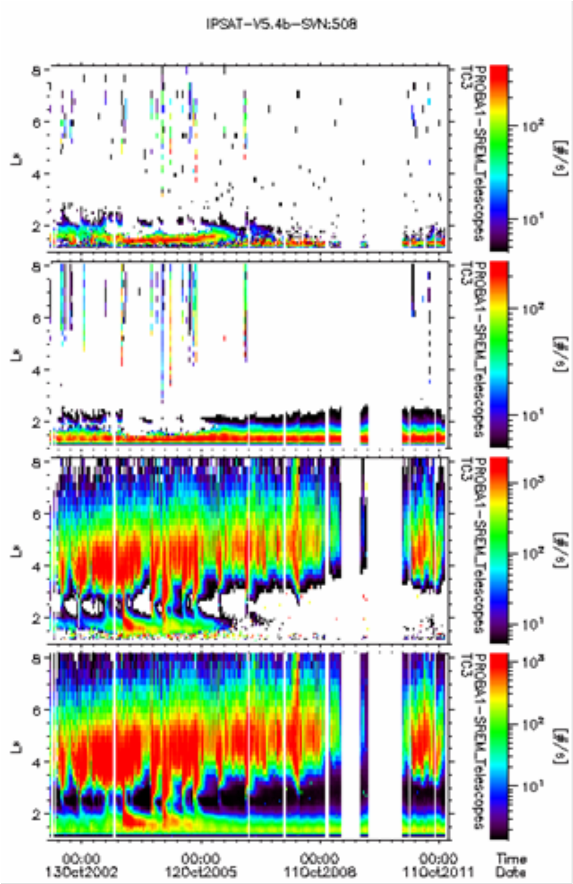

Figure 4: PROBA-1/SREM TC3 count rates in an L-shell versus time plot, with total count rates in the bottom panel, electrons only in the 2nd panel from bottom, protons only in the 3rd panel from bottom, and unknown in the top panel.

Next, the performance and capabilities of the ONERA data assimilation tool (which is in essence an ensemble Kalman filter) were enhanced. One of the major improvements regarding data assimilation itself has been to implement the capability of ingesting count rates data. To ensure a strong efficiency, this implementation is compliant with the CDF count rates file format adopted previously. The data assimilation tool has been implemented in such a way that it can retrieve the nature of data automatically. While the data assimilation tool is running the data to be assimilated and those used for validation are read from the database at the beginning of each day. Count rates, response function, L* and B/Beq are stored into a structure and are forwarded to the Kalman filter. During the analysis phase, 200 state vectors (members of the ensemble) of phase space densities (PSD) are used to evaluate each available measurement. Then 200 count rate predictions are available and can be compared to the real measure so that the Kalman filter can compute the update and drive the tool toward the true state of the radiation belts.

Another major improvement was the definition of a set of realistic boundary conditions at the outer edge of the electron radiation belts (L*=8). To do so, THEMIS/SST data have been used. Each unidirectional differential flux available have been correlated by pair (one pair being defined by the couple E, α_{eq} where E is the electron energy and α_{eq} its equatorial pitch-angle). The correlation matrix obtained is given in Figure 5, where each pixel represents a couple (E, α_{eq}). E_0 to E_{10} correspond to the 11 energy channels of THEMIS/SST: 31 keV, 41 keV, 52 keV, 65.5 keV, 92 keV, 139 keV, 203.5 keV, 293 keV, 408 keV, 565.5 keV and 719.5 keV and α_0 to α_3 correspond to the 4 equatorial pitch angles available in the data: 0-22.5°, 22.5-45°, 45-77.5°, 77.5-90°. In Figure 5, the diagonal represents the correlation coefficient of unidirectional differential flux at a given couple (E, α_{eq}) with itself so it is equal to 1.0. Then, the correlation coefficients between unidirectional differential fluxes at several equatorial pitch angles for a given energy are almost the same. Thus, according to Figure 5, it appears that correlation coefficients are more energy dependent than equatorial pitch angle dependent. It is also clear that the fluxes at low energies are poorly correlated with the fluxes at high energy. This tendency is more pronounced as magnetic activity increases.

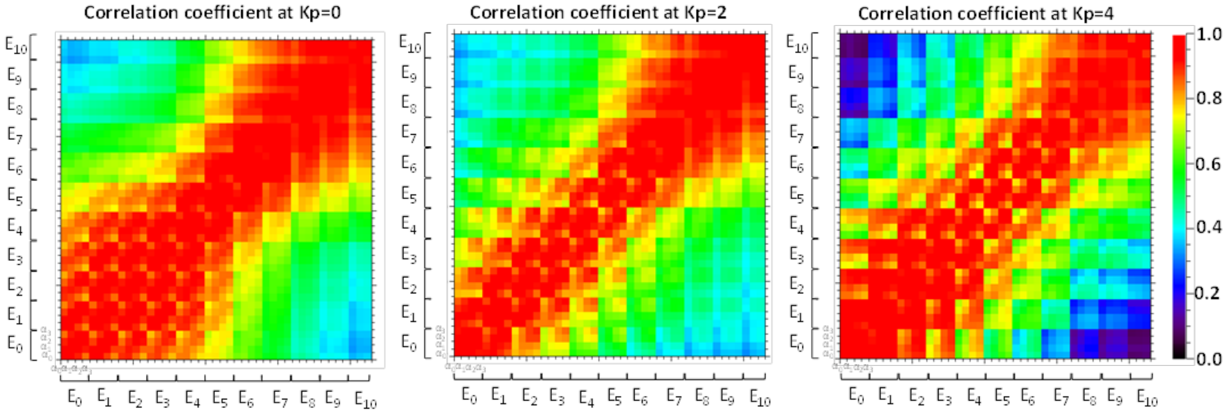

Figure 5: Correlation coefficients between the different energies for unidirectional electron flux and for three Kp values (Kp=0 on the left, Kp=2 in the middle and Kp=4 on the right). Details are provided in the RP2 report.

To generate a consistent and realistic set of boundary conditions, a set of tools able to generate Monte Carlo samplings that are correlated according to a given covariance matrix (deduced from the correlation matrix) have been developed. The Cholesky factorization of the covariance matrix was then used. In consequence, in the framework of an ensemble Kalman Filter (EnKF), one needs to perform as many samplings as there are members in the ensemble. Figure 6 highlights the energy spectra obtained as a boundary condition sampling for the EnKF if only the variance of each energy channel of SST (no correlation between each of them) are considered. There is clear evidence that such random oscillations between each energy channel may lead to unrealistic behaviour of the EnKF due to such a shape of the spectrum. On the contrary, Figure 7 presents the multi-variate sampling made using the whole variance-covariance matrix. The improvement is considerable, much more realistic and the spreading is still nicely distributed around the median spectrum. On both figures, the orange dashed line represents the 3 times the standard deviation above the median.

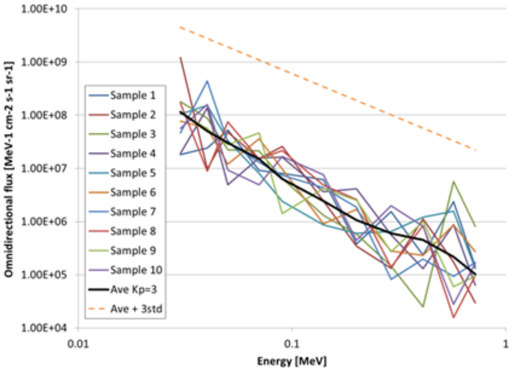

Figure 6: Example of a typical Monte Carlo sampling (10 spectra shown) of the boundary condition, when considering only the variance of each energy channel (no correlation taken into account). The median spectrum for Kp=3 is plotted in black, while the dashed orange line represents this median plus 3 times the standard deviation.

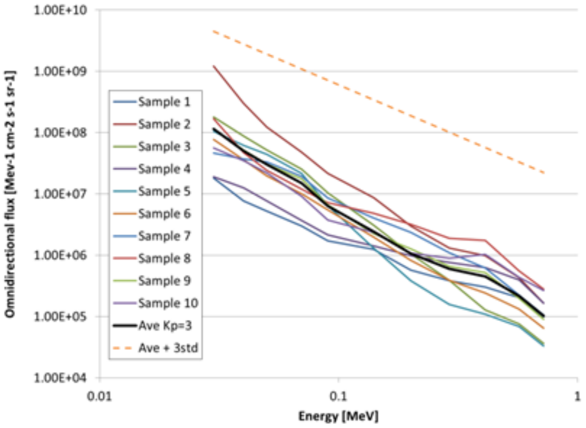

Figure 7: Example of the muli-variate Monte Carlo sampling of the boundary condition, when considering the whole variance-covariance matrix. The median spectrum for Kp=3 is plotted in black, while the dashed orange line represents this median plus 3 times the standard deviation.

To validate the results from the improved data assimilation tool, the time period from September 8, 2011 to September 25, 2011 was chosen. During this time period, two storms occurring with magnetic activity indices reaching Kp=6- and Dst=-70 nT and Kp=5+ and Dst=-70 nT, respectively. This time period was also chosen because of the good coverage of various data sets gathered in the particle database (i.e. GIOVE-B, INTEGRAL, GOES-13, XMM, THEMIS-A, B, C, D, E). This allows performing simulations with different configuration in term of data being assimilated and data being considered as test data.

Although GOES and GIOVE-B measures are assimilated, the principle of the Kalman filter does not guarantee that the measurements are reproduced exactly. The filter makes a balance between model predictions and measurements. The results clearly show that both GOES-13 and GIOVE-B measurements are reproduced by the Kalman filter with a high fidelity (see top panel in Figure 8). INTEGRAL/IREM data were not used in the assimilation process, so that this data set is a true third party one to validate the tool. Comparing the bottom two panels in Figure 8, one can see that the Kalman filter is quite powerful to restore INTEGRAL/IREM measurements. The energetic electron build-up during the recovery phase of the first storm as well as the drop out on September 17, 2001 are well reproduced. Looking in more details (see second panel from top in Figure 8), the Kalman filter over-predicts count rates for L*<4, i.e. in the slot region where there are very steep gradients. This is not surprising because no data are being assimilated for L*<4. This is to say that no objective details are provided to the filter to guide the model toward the true state other than the prediction from the pure physical radiation belt model. In the 4<L*<6 range, the predictions are very much similar to in-situ measurements. At large L* (specifically L*>6), the Kalman filter over-predicts INTEGRAL/IREM measurements. These differences are attributed to: (1) the magnetic field topology at large distances which can be distorted during active time (in the simulation, an IGRF+Olson Pfitzer quiet magnetic field is assumed); and (2) wave amplitudes are overestimated at L*>6.

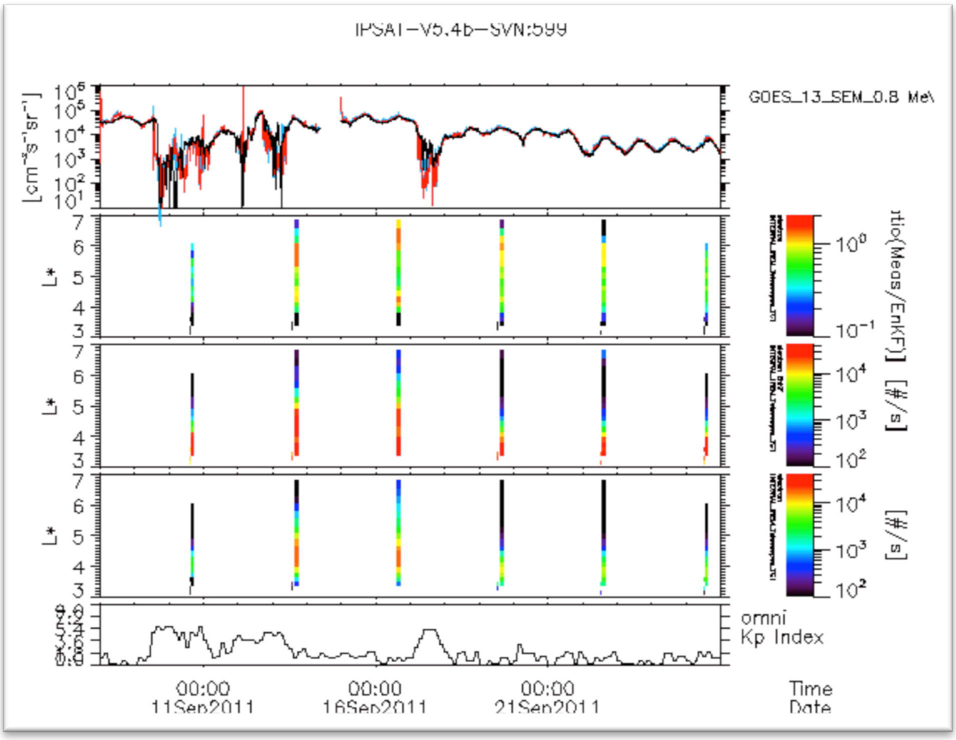

Figure 8: EnKF results when only two data sets are assimilated (i.e. GOES/SEM and GIOVE-B/SREM). Details provided in the RP2 report.

One of the most widely used and reliable methods of assessing a data assimilation scheme is that of the twin experiments. The identical-twin experiments consist in a numerical procedure where synthetic data can be generated by the model to which data assimilation is applied, subject to a specified stochastic forcing term. The data with assigned errors are then evaluated for their effectiveness in obtaining optimal state estimates. The convergence of the unassimilated model fields from the second run towards those of the first run (“true” state) can then be measured. Three different orbits have been chosen to investigate the data assimilation tool performances: two of them are operational orbits, geostationary and navigation orbits and the third one is a Geostationary Transfer Orbit (GTO). The metrics being set to evaluate the tool performance consists in computing the median and the standard deviation of the ratio between the predicted phase space density by the EnKF and the true phase space density for energies greater than 300 keV.

In conclusion, combining a radiation belt physical model and in-situ data via a data assimilation tool is very powerful to retrieve the global dynamic true state of the radiation belts. The analysis of the performance of the data assimilation tool clearly indicates that there is no need to have a bunch of data to assimilate to converge toward the true state. Even if one has only measurements along one GEO and one navigation (GPS) orbit, it will still be enough to drive the tool toward the true state with acceptable uncertainties. Of course, adding more input data to the system allows to improve the overall prediction, but one must be very careful to have well-distributed measurements in space (and energy) so as not to promote an orbit against another (otherwise, it would introduce bias).

3.2 ULF & VLF wave database

One of the main objectives of WP3 was to create a comprehensive database of VLF and ULF wave parameters from both space-based and ground-based measurements. The main requirements to the database are that the data from the different sources must be analysed in a similar way providing a specific set of wave parameters presented in the same coordinate system. All of these allowing for easy combination of data from different sources for further science analysis, as for example, for statistical wave models discussed later.

Table 1: Wave parameters provided by the MAARBLE Wave Databases.

Name	**Units**	**Description**
Time	ISO time	Time tags
Frequency	Hz	Interval centred frequency tag
Frequency_BHW	Hz	Frequency bin half widths
BB_xxyyzz_fac	$nT^2\ Hz^{-1}$	B Power spectral density
KSVD_fac	deg, deg	Direction of propagation (SVD): polar and azimuthal angles.
ELLSVD	Unitless	Ellipticity of the polarization (SVD). Range: -1..1.
PLANSVD	Unitless	Planarity of polarization (SVD). Range: 0..1.
POLSVD	Unitless	Degree of polarization in the polarization plane (SVD). Range: 0..1.
DOP	Unitless	3D degree of polarization defined in Samson (1973).
BMAG	nT	Magnitude of the DC magnetic field.
EE_xxyyzz_fac*	$mV^2\ m^{-2}\ Hz^{-1}$	E Power spectral density
EESUM_xxyy_isr2*		Sum of E Power spectral density in two measured components in the spacecraft spin plane
PV*,**	$W/m^2/Hz$, deg,	Poynting vector: amplitude, polar and azimuthal angles

*subject to availability of E measurement.
** for Pc3-5 we use zero parallel electric field approximation E.B=0. For higher frequencies we use dE·dB=0 (wave fields), which assumes presence of a single wave.

Table 1 provides a summary of parameters included in the datasets provided by the MAARBLE Wave Database, and which are described in detail later on. The polarization parameters are computed using the Singular Value Decomposition (SVD) technique and are defined in Santolik et al. (2003). The vector and tensor quantities are provided in the magnetic Field-Aligned Coordinate (FAC) system, which is defined as: **z**||**B**, **y** = **z** x **R**, **x** = **y** x **z.** For VLF/ULF datasets the transformation matrix from the spacecraft coordinates is provided as auxiliary datasets. The general datasets include space data for $3R_E<R<10R_E$ and magnetic latitudes up to 60°, i.e. focused on the region of space most important for wave-particle interactions affecting the radiation belts dynamics.

MAARBLE is using the **ESA Cluster Science Archive (CSA)** as a data distribution system for the wave database. This provides the highest possible level of sustainability of the database, and makes the database directly accessible to a wide science community using already existing tools and data formats. We have adapted the MAARBLE data products to the CSA format, and interacted with CSA staff on the details of dataset ingestion into the CSA. The datasets provided by the MAARBLE wave database are compliant to the CSA standards: Metadata dictionary and Cluster Exchange (CEF) file format (http://caa.estec.esa.int/caa/documentation.xml). The MAARBLE Wave Database datasets are available both in CEF and NASA Common Data Format (CDF) from the CSA (http://www.cosmos.esa.int/web/csa) as well as from a temporary data distribution via a server at IRF (http://www.space.irfu.se/data/caa/MAARBLE/WaveDatabase/). The IRF server also contains a set of summary plots used for validation of the produced datasets. The MAARBLE wave database includes datasets covering the *Very Low Frequency* (LVF) and *Ultra Low Frequency* (ULF) bands, described in detail below.

VLF database. VLF datasets (Deliverable 3.2) are based on the data from the ESA Cluster (4 spacecraft) and NASA THEMIS (5 spacecraft) missions. Cluster is ESA's cornerstone mission, operating since 2000 in the Earth's magnetosphere. Cluster provides the most comprehensive dataset available up to date for statistical magnetospheric studies, and in particular for studying waves. The Custer VLF products are based on the data from the STAFF-SA instrument, which provides spectral matrices of electric and magnetic field.

THEMIS data are complementary to Cluster, as they provide high-resolution waveform measurements of vector electric and magnetic fields, which are not available on Cluster. Even coverage of such data is very limited compared to Cluster; it provides important information necessary to characterize the waves observed in the ULF range. Moreover, Cluster and THEMIS have very different orbit planes (Cluster: polar, THEMIS: equatorial), and therefore combined they provide good coverage of the regions where wave-particle interactions affect the radiation belt particles. A total of 79499 files have been delivered to the CSA for the VLF database.

ULF wave database. ULF waves play an important role in radiation belt dynamics, being responsible for diffusion as well as for energization and losses of electrons. The Wave Database in the ULF, Pc-1 down to Pc5, frequency range (Deliverable 3.2) provide data from the following sources ranging from the outer magnetosphere down to ground-based stations:

- Cluster (4 spacecraft),
- THEMIS (5 spacecraft),
- GOES (2 spacecraft),
- CHAMP (1 spacecraft)
- IMAGE (10 ground stations)
- CARISMA (5 ground stations)

We have delivered a total of 167301 to the CSA containing ULF datasets as part of the MAARBLE Wave Database. The software used to produce a major part of the ULF database is publicly available as part of the IRFU-MATLAB package via GitHub (https://github.com/irfu/irfu-matlab). The **space-based part of the ULF database** covers the entire magnetosphere over almost a complete solar cycle. It is based primarily on the Cluster measurements for years 2001-2011, which is complemented by THEMIS (2007-2011) and GOES (2007-2008), as well as by the CHAMP spacecraft in low-Earth orbit - LEO (2001-2010). The **ULF ground-based database** is an important complement to the space-based database. The database includes 10 ground stations of the IMAGE network in Europe for years 2000-2010 (station codes: DOB, HOR, KEV, KIR, NUR, OUJ, RVK, SOD, TRO, UPS) as well as 5 ground stations of the CARISMA network in the northern America for years 2005-2013 (station codes: FCHU, GILL, ISLL, PINA, RANK).

3.3 Statistical models of wave activity

The next step after creating the wave database is to mine the database in order to create statistical models of wave activity for different types of waves. These models, or *statistical maps*, constitute deliverable 3.3. Their main goal is to determine statistical distribution of not only amplitudes, but also wave normal angles and other polarization and propagation characteristics, which determine how the waves interact with particles.

VLF maps – Statistics of lower-band whistlers. Lower-band whistler-mode emissions can influence the dynamics of the outer Van Allen radiation belts. We have used 11 years of measurements of the STAFF-SA instruments on-board the four Cluster spacecraft to systematically build maps of wave propagation parameters as a function of position. We have determined probability distributions of wave vector angle weighted by the wave intensity. The results show that wave vector directions of intense waves are close to a Gaussian-shaped peak centred on the local magnetic field line. The width of this peak is between 10 and 20 degrees. The cumulative percentage of oblique waves is below 10-15%. This result is especially significant for an important class of whistler-mode emissions of lower-band chorus at higher latitudes, well outside their source region, where a simple ray tracing model fails and another mechanism is necessary to keep the wave vectors close to the field-aligned direction (Figure 9).

VLF maps – Statistics of banded whistlers. Characteristics of banded whistler-mode emissions have been derived from a database of chorus-like events obtained from the complete data set of the wave measurements provided by the STAFF-DWP wave instrument on-board the TC-1 spacecraft (Figure 10). Our study covers the full operational period of this spacecraft (almost four years). Our entire data set has been collected within 30 degrees of geomagnetic latitude at L-shells between 2 and 12 and below 4 kHz. All events have been processed automatically to accurately determine their power spectral density (PSD), bandwidth and amplitude. We found most cases of chorus-like banded emissions at L<10 on the dawnside and dayside. The upper band emissions (above one half of the equatorial electron cyclotron frequency) occur almost twenty times less often than the lower band and their average amplitude is almost three times less than for the lower band. Intense upper band emissions cover smaller L-shell, MLT and magnetic latitudes regions than intense lower band emissions. The intense nightside and dawnside chorus-like banded emissions were observed at low magnetic latitudes, while the intense dayside and duskside emissions were mostly found at higher magnetic latitudes. The amplitudes of dayside lower band slightly increase as they propagate away from the geomagnetic equator and are smaller than chorus amplitudes on the nightside and dawnside. The PSD, the amplitude of the lower band and its frequency bandwidth and its occurrence rate significantly increase with increasing geomagnetic activity, while all these parameters for the upper band are not so strongly dependent on a variability of the geomagnetic activity.

VLF maps – Statistics of whistler mode chorus rising and falling tones. We conducted a study of wave normal angles (θ_k) of whistler mode chorus emission as observed by THEMIS during the year 2008. The three inner THEMIS satellites THA, THD, and THE usually orbit Earth close to the dipole magnetic equator ($\pm 20^\circ$), covering a large range of L shells from the plasmasphere out to the magnetopause. Waveform measurements of electric and magnetic fields enable a detailed polarization analysis of chorus below 4 kHz. When displayed in a frequency-θ_k histogram, four characteristic regions of occurrence are evident (Figure 11). They are separated by gaps at $f/f_{ce} \approx 0.5$ (f is the chorus frequency, f_{ce} is the local electron cyclotron frequency) and at $\theta_k \sim 40^\circ$. Below $\theta_k \sim 40^\circ$, the average value for θ_k is predominantly field aligned, but slightly increasing with frequency toward half of f_{ce} (θ_k up to 20°). Above half of f_{ce}, the average θk is again decreasing with frequency. Above $\theta_k \sim 40^\circ$, wave normal angles are usually close to the resonance cone angle. Furthermore, we present a detailed comparison of electric and magnetic fields of chorus rising and falling tones. Falling tones exhibit peaks in occurrence solely for $\theta_k > 40^\circ$ and are propagating close to the resonance cone angle. Nevertheless, when comparing rising tones to falling tones at $\theta_k > 40^\circ$, the ratio of magnetic to electric field shows no significant differences. Thus, we conclude that falling tones are generated under similar conditions as rising tones, with common source regions close to the magnetic equatorial plane.

VLF maps – Statistics of equatorial noise. We have also reported results of a systematic analysis of equatorial noise (EN) emissions, which are also known as fast magnetosonic waves. EN occurs in the vicinity of the geomagnetic equator at frequencies between the local proton cyclotron frequency and the lower hybrid frequency. Our analysis is based on the data collected by the STAFF-SA instruments on board the four Cluster spacecraft. The data set covers the period from January 2001 to December 2010. We have developed selection criteria for the visual identification of these emissions and we have compiled a list of more than 2000 events identified during the analysed time period. The evolution of the Cluster orbit enables us to investigate a large range of McIlwain's L parameter, from L=1.1 to =10. We demonstrate that EN can occur at almost all analysed L-shells. However, the occurrence rate is very low (<6%) at L-shells below L=2.5 and above L=8.5. EN mostly occurs between L=3 and L=5.5, and within 7^o of the geomagnetic equator, reaching 40% occurrence rate. This rate further increases to more than 60% under geomagnetically disturbed conditions. Analysis of occurrence rates as a function of magnetic local time (MLT) shows strong variations outside of the plasmasphere (with a peak around 15 MLT), while the occurrence rate inside the plasmasphere is almost independent on MLT.

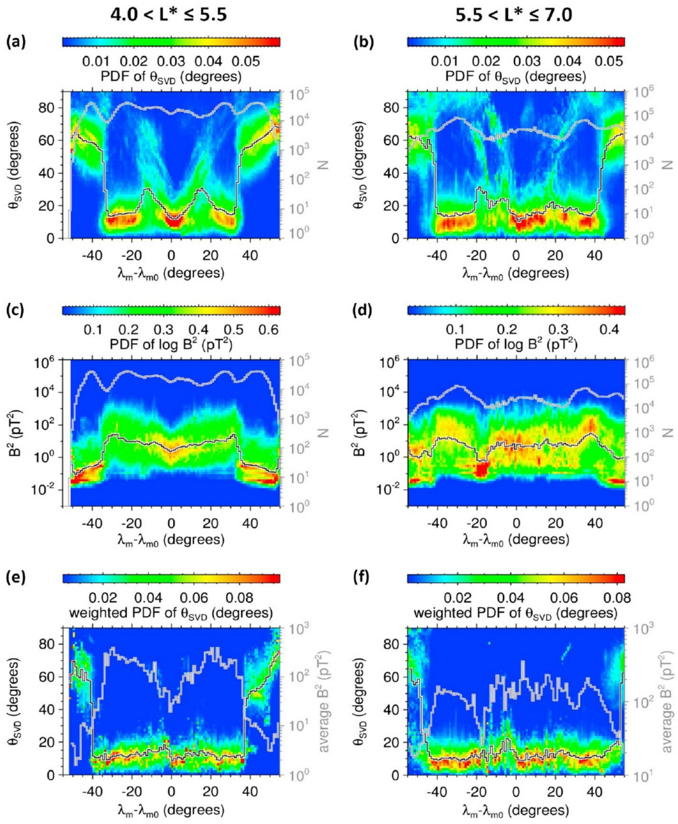

Figure 9: Analysis of wave propagation in the frequency band 0.1–0.5 electron cyclotron frequency as a function of the magnetic latitude. Details provided in D3.3.

ULF maps – Amplitude distribution and propagation properties of EMIC waves: a statistical map from Cluster and THEMIS. We perform a statistical study of occurrence and propagation properties of EMIC waves in the Earth's magnetosphere. EMIC wave events are found using an automated wave selection routine. This is the first study combining EMIC data from multiple missions; we use data from both Cluster and THEMIS to construct a comprehensive map of EMIC waves with good coverage in both MLT and mLat (Figure 12). The conclusions from this statistical study are: (1) An off-equatorial population of EMIC waves exists. This is a significant population, which has not previously been reported on. (2) When the EMIC wave occurrence is separated into hydrogen, helium, and oxygen bands, it is seen that each band is prevalent in a different region from the other bands. The hydrogen band has highest occurrences in the morning sector, the helium band has highest occurrences in the afternoon sector, and the oxygen band has the highest occurrences on the dusk side. (3) The statistics of EMIC wave parameters have been presented, including wave amplitude, wave vector direction, and ellipticity. The wave vector direction is strongly aligned with the background magnetic field. The wave amplitude has a distribution over a range of values. For dayside, nightside, and equatorial events the highest peak value occurs in the oxygen band, and the helium and hydrogen bands having similar peak values. In the off-equatorial events, the peak amplitude does not vary much in the three different bands. The ellipticity is more strongly left-handed in the dayside and equatorial events. In the nightside, the ellipticity of oxygen band events is predominantly right-handed.

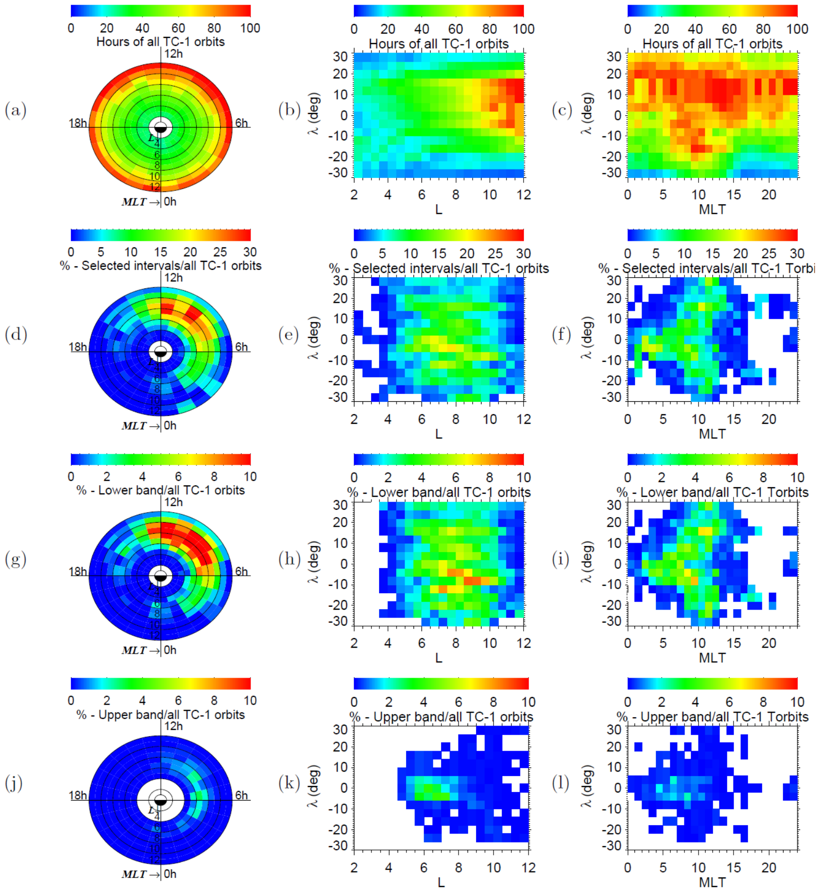

Figure 10: Maps of banded whistler-mode emissions. Details provided in D3.3.

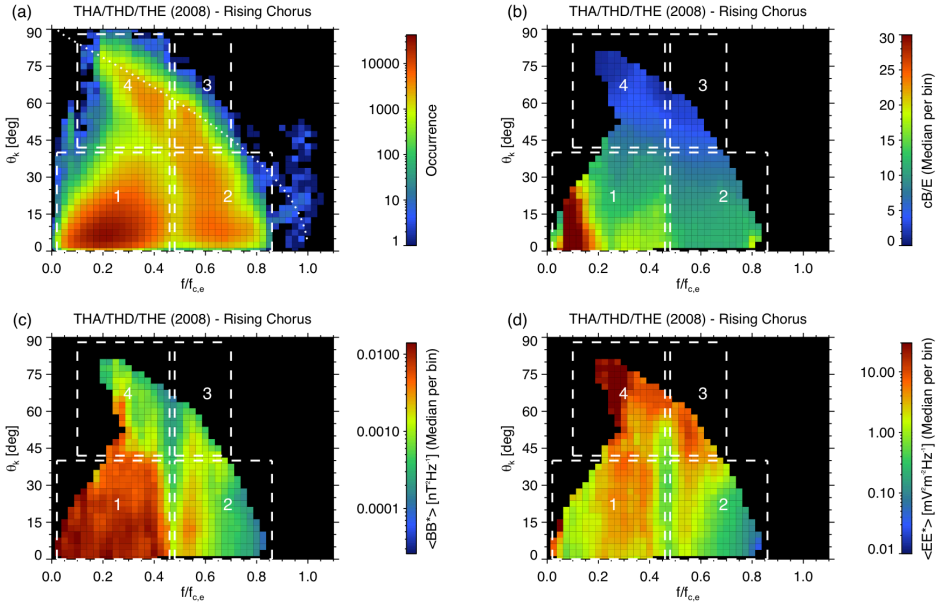

Figure 11: Maps of whistler mode chorus emissions. Details provided in D3.3

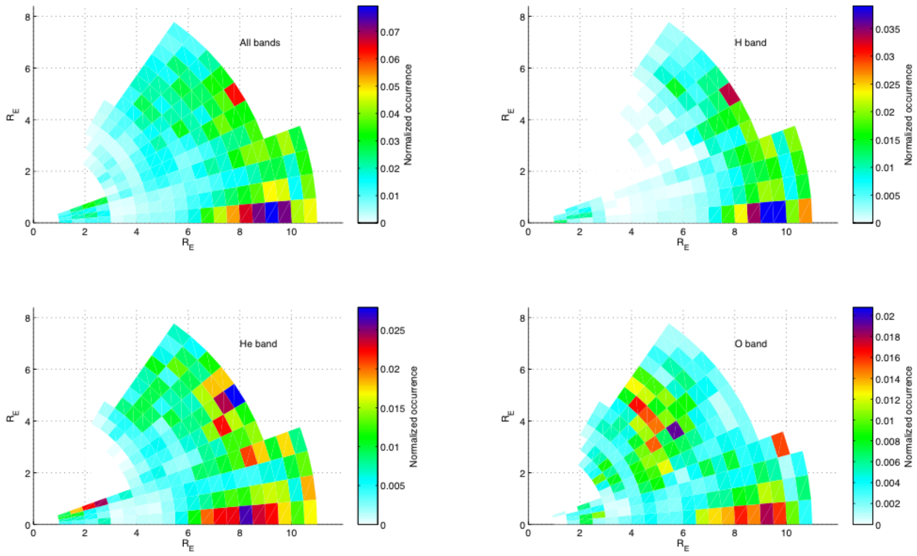

Figure 12: Normalized occurrence of EMIC waves. Details provided in D3.3.

ULF maps – 3-D distribution of ULF wave power in the inner magnetosphere (Pc3-5 band). We use the ULF wave power spectra densities (PSDs) for Cluster and THEMIS satellites available from the MAARBLE wave database. In this statistical study, a one-minute value of PSD is considered as a data sample. The square roots of the integral of the power spectral density over each frequency ranges (hereinafter referred to as 'wave power') are used to measure the intensity of the ULF wave oscillation, as defined as,

$$\delta E_r = \left(\int_{f_1}^{f_2} PSD\_E_r(f)df \right)^{1/2}, \delta E_\varphi = \left(\int_{f_1}^{f_2} PSD\_E_\varphi(f)df \right)^{1/2}$$

for radial and azimuthal electric field in the Mean Field Aligned coordinate system, respectively. The integration intervals are for Pc5, Pc4 and Pc3 bands, respectively. Figure 13 illustrates the three dimensional distribution of Pc3-5 ULF wave power of radial electric field. Pc5 ULF wave power in the equatorial plane (left-bottom panel) is generally stronger in the high-L region than in the low-L region, and stronger in the dayside than in the nightside. These are consistent with the scenario that the external generation sources, e.g. K-H instability and dynamic pressure variation, dominate the ULF wave generation and the energy transfer through the magnetopause into the magnetosphere in the form of ULF waves. There is also more power in the pre-midnight sector than in the post-midnight sector, which could be possibly related to substorm activity in the magnetosphere. Similar pattern of Pc4 ULF wave power near the magnetic equator plane (left-middle panel) can be seen as compared with Pc5 power, except that Pc4 power distributed more inside than Pc5 power. This could be related to the fact that the eigenfrequency of magnetic field lines increases from magnetopause to plasmapause. Pc3 wave power (left-top panel) is mostly distributed in the dayside near the magnetopause, because the majority of Pc3 waves are propagate from the ion foreshock region in front of the bow shock.

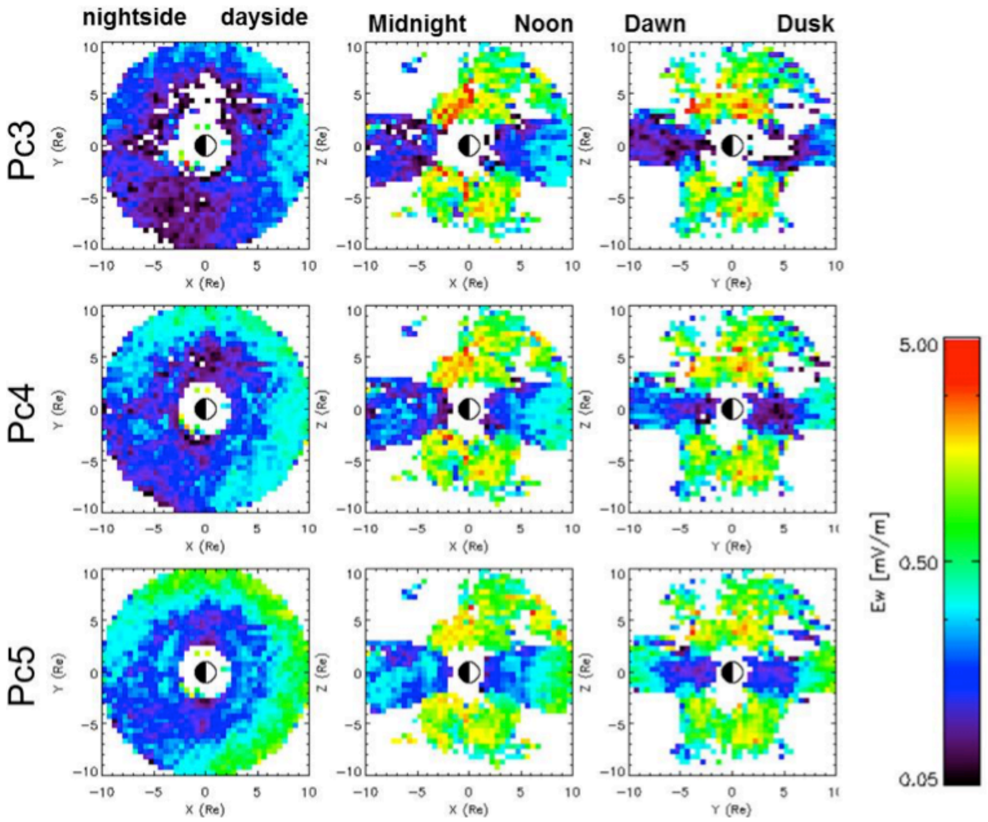

Figure 13: Distribution of ULF wave power in radial electric field component, with Pc3, Pc4 and Pc5 from top to bottom and x-y, x-z and y-z planes from left to right. Details provided in D3.3.

3.4 Physics-based ULF wave radial diffusion

Radial diffusion, generated by ULF waves, is thought to play an important role in the transport of electrons in the outer radiation belt. In situ measurements of those waves' power spectral densities would require a large number of satellites operating in different orbits, which is currently prohibitively expensive. As a more practical alternative, measurements from ground-based magnetometers can be continuously taken and then mapped to their equivalent L-shells in the equatorial plane.

The overall diffusion coefficient is the sum of the diffusion coefficients due to the electric and compressional magnetic field perturbations, which are functions of the ULF wave power spectral density of the electric and magnetic field perturbations with azimuthal wave-number m at wave frequencies ω satisfying the drift resonance condition. Since ω_d is a function of the electron's energy and L-shell, this introduces an energy and L-shell dependence into the PSD terms. One of the major accomplishments of MAARBLE was to use ground-based and satellite measurements to determine the electric and magnetic fields in space and hence characterise the statistical response to ULF waves based on solar wind or geomagnetic drivers.

Ground-based Determination of Electric Diffusion.

In order to determine the electric field diffusion coefficient the azimuthal electric PSD in space in the equatorial plane as a function of wave and m-*value* must be known. To directly measure the required electric and magnetic field PSDs and wave *m*-values would require multiple simultaneous measurements of the global structure and variability of the wave's electric and magnetic fields in space in the equatorial plane. However, this would require the deployment of multi-satellite constellations in the radiation belt region. Instead of using in-situ measurements of electric field PSD, to determine ULF wave driven diffusion coefficients we use ground-based magnetometer measurements to obtain the magnetic PSD on the ground, and map these magnetic field PSDs to the electric field PSD in space in the equatorial plane using the Alfvénic wave mapping model. In the MAARBLE project we derived a series of models.

For this task we first used the same database of hourly PSD estimates taken using the CARISMA and SAMNET magnetometer stations over a period of approximately 15 years. However, here we determined the median D-component PSDs binned with Kp and solar wind speed using the hourly PSD estimates derived for windows 1 hour in length taken only from the dayside between 0600 LT and 1800 LT. The median azimuthal electric field PSD, P_{total}^{E} in space in the equatorial plane as a function of Kp or solar wind speed, derived from the ground-based magnetometer measurements of fits to the mapped ULF D-component. By combining these expressions for the electric field PSD analytic expressions for the electric field diffusion coefficients can be obtained. This approach assumes that the all of the ULF wave power is contained in a single wave m-value. Typically it is assumed that this m-value is m=1, however changing the assumed m-value to m=10 has little effect on the diffusion coefficients (Figure 14).

Alternatively, a much simpler analytic expression for the electric field diffusion in units of days^{-1} was also derived in the MAARBLE project. The PSD, P_{total}^{E} was determined as a function of frequency, L-shell and Kp and analytic fits, P_{total}^{Efit} derived to give these values as a function of L-shell and Kp, with no frequency dependence (see RP2 for more details):

$$P_{total}^{Efit} \approx \sum_{m}^{\infty} P_{m}^{E} = 10^{0.208L+0.457Kp-4.68}$$

Approximating the PSD to a simple function of L-shell and Kp which represent functional dependence that is effectively independent of frequency allows the generation of a simple yet powerful analytic expression for the electric field diffusion coefficients to be derived such that:

$$D_{LL}^{E} = 5.75\times10^{-9}\times L^{6}10^{0.208L+0.457Kp}$$

Here the diffusion coefficient D_{LL}^{E}, is expressed in terms of days. Analysis also showed values of D_{LL}^{E} corresponding to the upper and lower quartile PSD values can also be approximated by multiplying or dividing diffusion by a factor of 3 respectively and this can be used to provide a measure of uncertainty in modelling such that Kalman filter approach in WP2.

Within the MAARBLE project, we also validated the analysis from the Canadian sector by additionally using data from Europe to ensure that the assumptions relating to global ULF wave power can be derived from a single geographic meridian from the IMAGE array. In order to examine a wider range of solar wind drivers than the Kp and solar wind speed described above, we have processed the measurements with four binning methods, as functions of Kp, Dst, solar wind speed and solar wind pressure. Upper and lower quartiles were calculated for all initial values and derived diffusion coefficients, and the PSDs were analyzed by deciles, in which case Kp was found to be the best single parameter for predicting the effect of ULF wave power in radial diffusion. Binning by Dst, however, reveals a remarkable high-energy tail in the ULF wave power distribution (panel (b) of Figure 15). This is more pronounced for lower L stations than for higher L ones, which lends further credence to observations that ULF wave power penetration to low L is connected with decreases in Dst.

Magnetic Diffusion Coefficients

Since the compressional fast wave fields in the magnetosphere in general depend on all the wavenumbers in their dispersion relations, it is difficult to estimate in-situ equatorial compressional fields using ground data. Indeed, mapping approaches produce results, which are not a good representation of the in-situ data. Instead we use empirical statistical characterizations of compressional PSD based on in-situ PSD measured in space.

The required compressional magnetic field PSDs in the equatorial plane at *L*=6.7 are calculated here each hour using GOES East and West data from 1996 to 2005. The GOES magnetic field measurements have been rotated into a field-aligned coordinate system using the same method of Rae et al. (2005), apply a 30 minutes running mean. Similar to the ground magnetic field PSD analysis, the median in-situ compressional wave PSDs are determined and binned with Kp and solar wind speed. However, the in-situ PSD values used as input for driving D_{LL}^{B} are determined by averaging over 24 hrs MLT, as opposed to the ground magnetic magnetometer PSD values for D_{LL}^{E} which are averaged over the dayside from 0600 LT to 1800 LT. However, to determine the magnetic field PSD at different L-shells the GOES PSD results are supplemented with THEMIS measurements of the compressional magnetic field PSD at *L*=4, *L*=5, *L=6* and *L*=7. For the THEMIS results a 20 minutes window length was used and the background magnetic field was removed by applying a 20 minutes running mean. By merging these GOES and AMPTE data sets we characterised the compressional magnetic field PSD with L-shell and Kp or solar wind speed.

Each of these magnetic field PSD values has been fitted to an analytic function of the form

$$P_{total}^{Bfit} \approx \sum_{m}^{\infty} P_{m}^{B} = B(L,Kp)f^{-2} \tag{1}$$

where $B(L,Kp) = 10^{L^{2}0.1115+LK_{p}0.0824-L1.3193+K_{p}{}^{2}0.0291-K_{p}0.2700-19.4002}$

Based on our fits to the GOES and THEMIS compressional magnetic field PSDs, the magnetic diffusion coefficient in units of days^{-1} can then be expressed analytically as

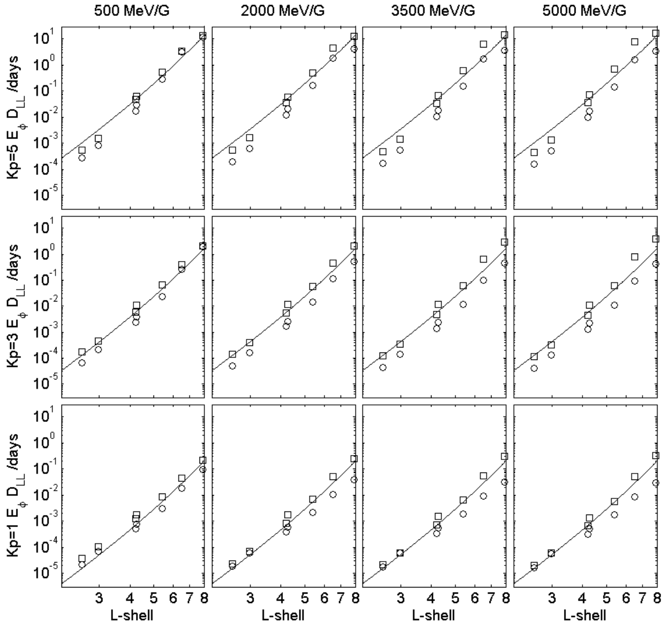

Figure 14: The symbols represent azimuthal electric field diffusion coefficients derived directly from the mapped ground PSD measurements (see Figure 4 of Ozeke et al., 2012) and assuming wave m-values of *m*=1 (squares) and *m*=10 (circles).

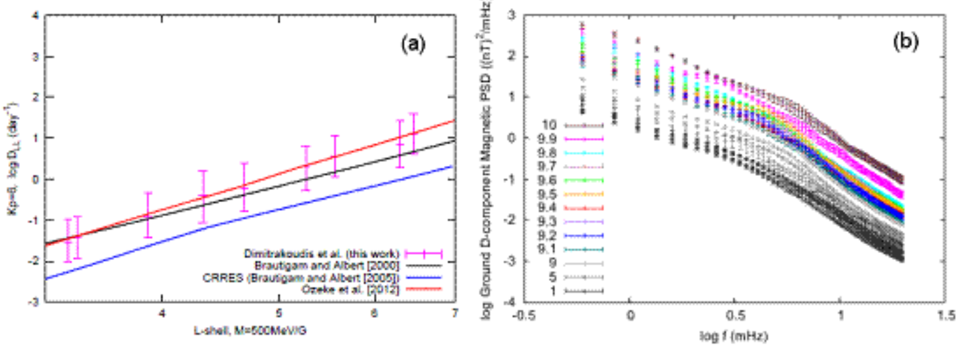

Figure 15: a) A comparison of the electric field diffusion coefficients found in our work with the ones in previous publications. b) Median magnetic field D-component power spectral densities as measured at Tromsø station (L=6.46), binned by Dst. The top decile is further split into deciles (colored data points, denoted by 9.1 - 10). The lower nine deciles are plotted in grey scale.

$$D_{LL}^{B} = 1.94\times10^{-6} L^{8} 10^{L^{2}0.112 + LK_{p}0.0824 - L1.32 + {K_{p}}^{2}0.0291 - K_{p}0.270} \qquad (2)$$

Figure 16 shows that our m-value and energy independent diffusion coefficients are in good agreement with those derived directly from the GOES and THEMIS measured PSD values. From the perspective of modelling radial diffusion, it turns out that for specific conditions the magnetic diffusion coefficients are typically much smaller than the electric ones such that the magnetic diffusion can be neglected which makes the simulation of the ULF wave radial diffusion much simpler. Figure 17 below shows an example of the results of a ULF wave radial diffusion simulation, driven by observed outer boundary conditions at the edge of the simulation and the new ULF wave diffusion coefficients derived with the MAARBLE project and published in GRL in 2014. As can be clearly seen the agreement is excellent.

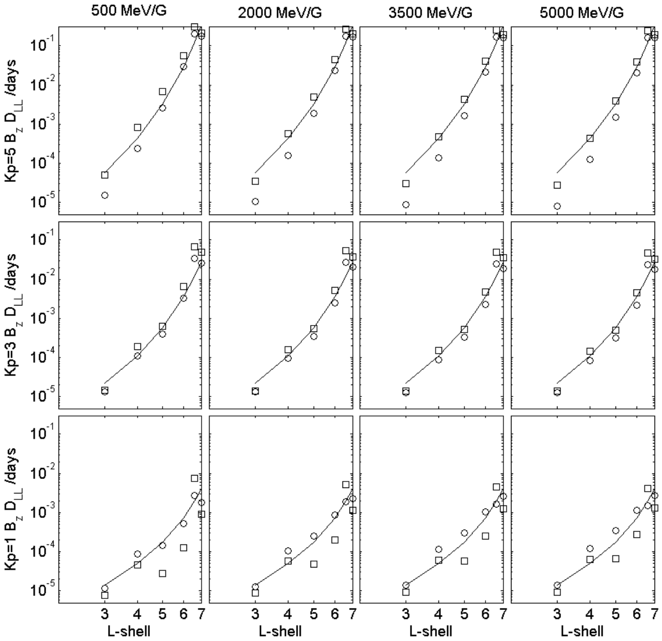

Figure 16: The symbols represent magnetic diffusion coefficients derived directly from the THEMIS and GOES PSD measurements, and assuming wave m-values of *m*=1 (squares) and *m*=10 (circles). The solid curve represents the magnetic diffusion coefficients derived from the magnetic PSD fits.

3.5 Coherent ULF wave impacts on radiation belt electrons

Coherent ULF waves are also hypothesised to affect radiation belt populations when their bandwidth is small and their amplitudes large. The project used very high-energy resolution data from the NASA Van Allen Probes mission to seek examples of such coherent, rather than diffusive interactions. The team also searched the THEMIS database from the SST instrument, but perhaps due to limits on the upper energy range and more likely due to the lower energy resolution, we did not find clear examples in the THEMIS dataset. However, the cleanliness of the Van Allen Probes data allowed us to discover the smoking gun of the action of a coherent geophysical synchrotron, which we then published in Nature Communications. Figure 18 shows the highlight of the outcome of that work.

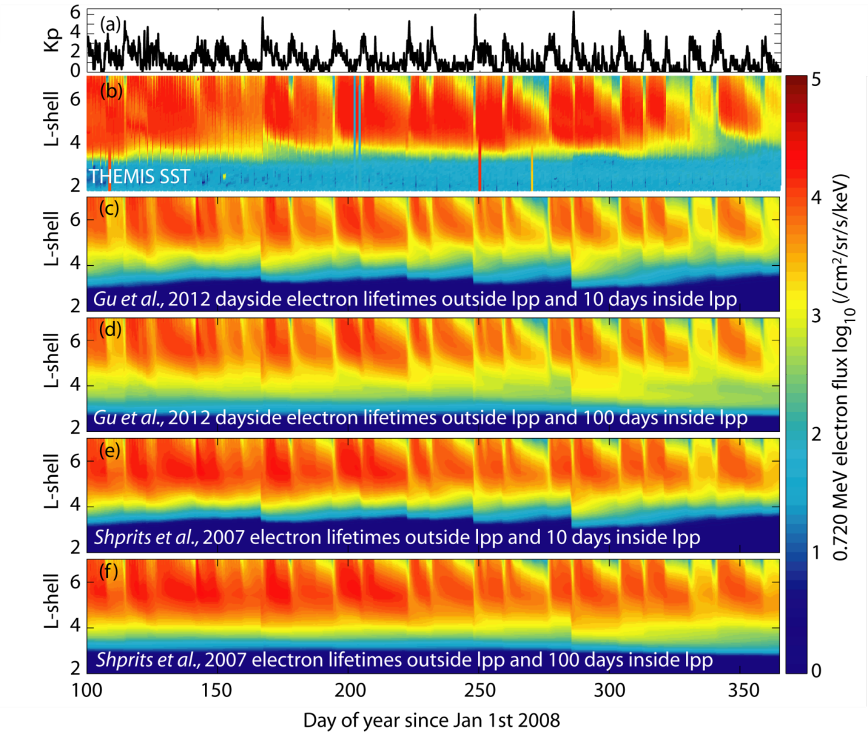

Figure 17: Comparison of THEMIS observation of 720 keV electrons with the output from the MAARBLE ULF wave-driven radial diffusion model. Losses are also included as defined by whistler modes outside a Kp dependent plasmapause by Shprits et al. (2007) and Gu et al. (2012).

3.6 EMIC and VLF waves' role in electron losses

Geospace magnetic storms, driven by the short-term solar wind variability, are associated with either increases or decreases of the fluxes of relativistic electrons in the outer radiation belt. Two important hypothesized loss processes are interactions and scattering of electrons into the atmosphere by lower band chorus (often labelled as VLF waves) as well as with higher frequency electromagnetic ion cyclotron (EMIC) waves. In the MAARBLE project we expended significant effort in characterizing the spatial structure of these waves, and their statistical variation with various solar wind drivers as well as analysing their spatial widths and association with cold plasma structures in the magnetosphere such as the plasmapause, in plasmaspheric plumes, or in the plasmatrough. The non-linear nature of various plasma wave bursts, and their connection to tail Earthward flows and compressions of the magnetosphere were also conducted. The outcomes from this work are extensive and described in detail in the published journal papers which resulted, and which are summarized in the reports for the work packages. For example, the in-situ data showed that EMIC waves were typically confined to narrow L-shell confined structures in the inner magnetosphere, usually just inside the plasmapause, even though ducting in the ionospheric waveguide can allow them to be seen long distances away from their source region on the ground. Interestingly, this likely contributes to some degree to the low occurrence rates of EMIC waves in satellite data. For example, Mann et al. (2014) using conjugate in-situ Van

Allen Probe and CARISMA ground-based magnetometer data show that on the elliptically orbiting satellites the waves appear to only last for about 10 minutes, while on the ground they are seen to persist for many hours courtesy of ducting to the magnetometer station on the ground from the narrow and continuous wave source in space!

One of the most exciting results is the discovery for the first time of evidence for the action of EMIC waves in causing the loss of MeV electrons from the Van Allen belts. Indeed, using the statistical characterization of the waves models also concurred with the identified EMIC loss hypothesis. However, perhaps most interesting was the conclusion that the EMIC waves could only interact with the low pitch angle particles, even at ultra-relativistic energies, such that whilst there was clear evidence that low pitch-angle particles were being scattered into the atmosphere, the core of the distribution where the peak of the flux resides was essentially unaffected.

In the framework of the MAARBLE project, we were also then able to bring multiple losses impacts from for example scattering into the atmosphere in EMIC and VLF waves, as well as acceleration and transport in ULF wave fields, to examine the response of relativistic electrons to selected magnetic storms and compare these with concurrent observations of ULF waves from the trans-Scandinavian IMAGE magnetometer network and magnetic stations collaborating in the worldwide SuperMAG project. The latitudinal and global distribution of Pc5 wave power is examined to determine how deep into the magnetosphere these waves can penetrate (Figure 19).

We also investigated the role of Pc5 wave activity deep in the magnetosphere in enhancements of radiation belt electrons population observed in the recovery phase of the magnetic storms. Specifically, the magnetic storm on 31 March 2001 was characterized by increased post-storm electron fluxes as compared to their pre-storm values. The inward shift of the peak and inner boundary of the outer electron radiation belt follows the Pc5 wave activity reaching L shells so low as 2. Our observations provide support for the hypothesis that enhanced Pc5 ULF wave activity during the main and recovery phase of magnetic storms can discriminate between storms that result in increases of relativistic electron fluxes in the outer radiation belts from those that do not. Particularly, Pc5 wave activity penetrating deep in the magnetosphere is common among magnetic storms with enhanced fluxes of relativistic electrons in the outer radiation belt.

Similar studies of the overall response of the belts to multiple acceleration and loss sources were also completed within MAARBLE using not only the Salammbo code described earlier, but also the BAS code. In this way, the details of the excitation and properties of the plasma waves, and their variations during storms, are brought together to determine the overall response of the radiation belts under the action of the delicate and competing balance between transport, acceleration, and loss.

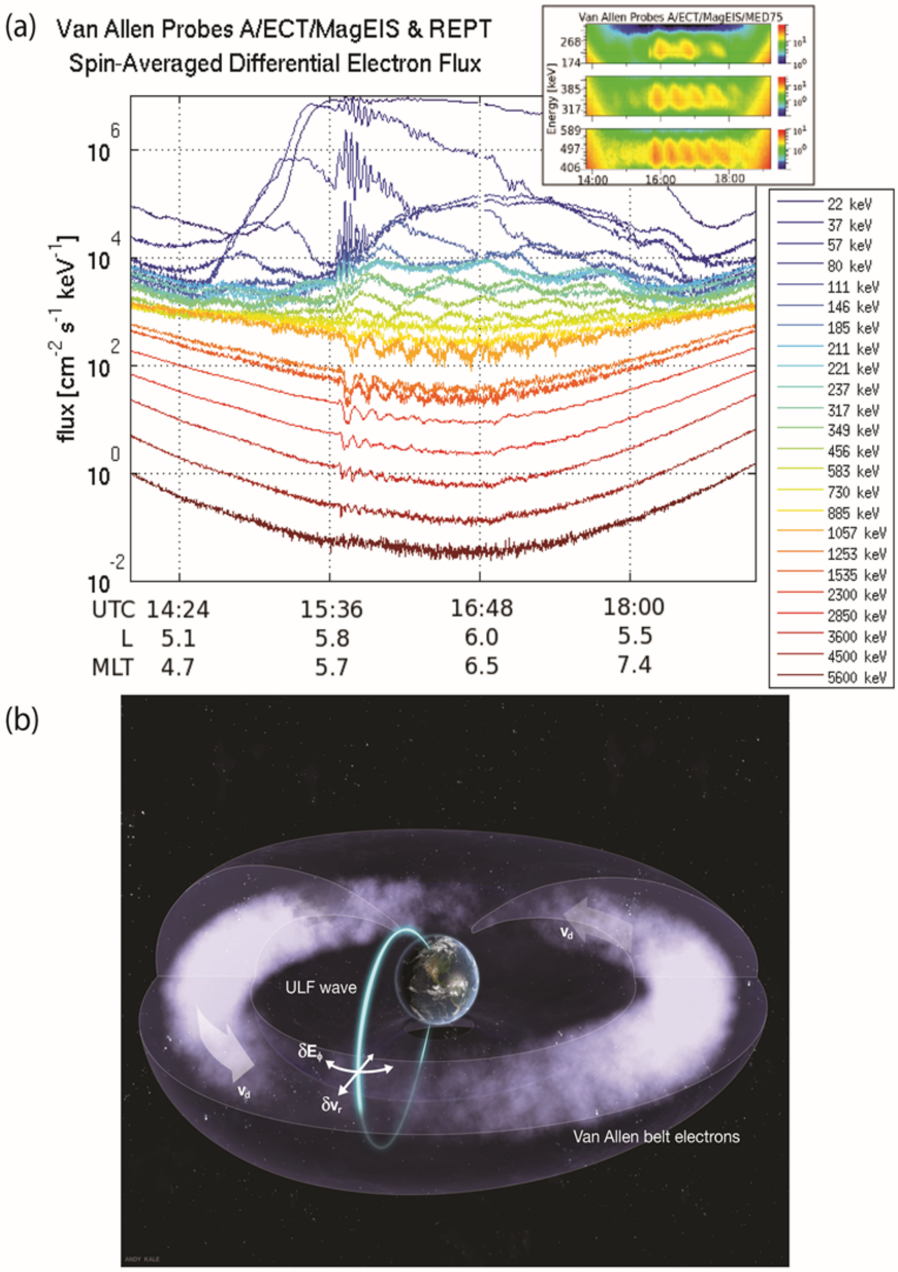

Figure 18. (a) Coherent ULF wave interactions revealed by modulation of the MeV energy electron flux observed by Van Allen Probe A. (b) Schematic of the resonant and coherent interaction between the ULF waves and the relativistic electrons in the belt.

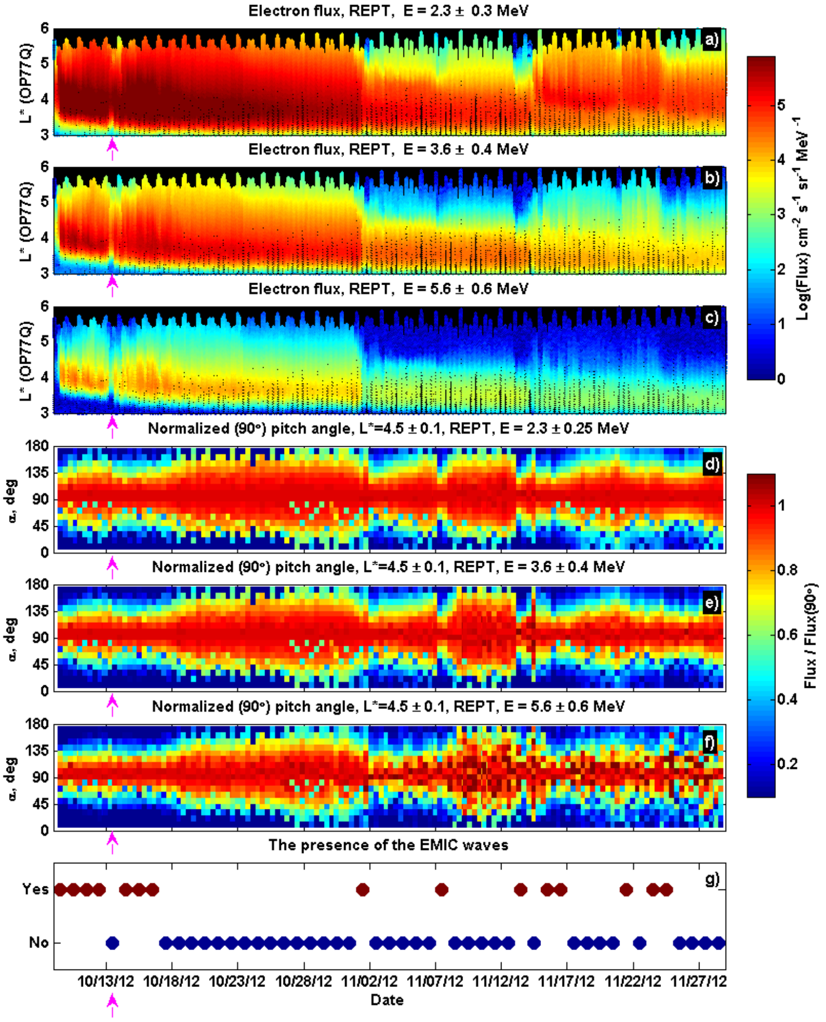

Figure 919. Flux as a function of L* (top three panels) and flux normalised to 90 degree pitch angle (PA) flux at L*=4.2 (next three panels) for three different ultra-relativistic energies. Bottom panel shows the occurrence of EMIC waves as determined from ground-based magnetometers around L=4.2 (from Usanova et al., 2014). Clear evidence of the loss of low PA particles is seen during intervals of EMIC wave occurrence demonstrating EMIC scattering loss of these low PA particles into the atmosphere.

4. Impact of the MAARBLE project

The MAARBLE project outcome already has and will continue to have a number of important impacts:

- MAARBLE has developed a standardized radiation belt electron database based on data from eight European spacecraft (XMM/ERMD, INTEGRAL/IREM, PROBA-1/SREM, GIOVE-B/SREM and CLUSTER/RAPID – 1 to 4) and from seven US spacecraft (THEMIS/SST – A, B, C, D, E, POLAR/CEPPAD and GOES/SEM). Furthermore, MAARBLE produced an extensive database containing characteristic properties of ULF and VLF electromagnetic waves in the magnetosphere. We have used space data from ESA/Cluster, ESA/CHAMP, ESA/Swarm, NASA/THEMIS and NOAA/GOES and ground-based magnetometer data from the CARISMA and IMAGE arrays. MAARBLE has taken care of the best possible access to the data for the whole scientific community: both databases are publicly available at http://craterre.onecert.fr/MAARBLE/ and at http://www.cosmos.esa.int/web/csa (the Cluster Science Archive) respectively.
- MAARBLE combined the electron database with a radiation belt physical model and showed the power of data assimilation in retrieving the global dynamic true state of the radiation belts.
- MAARBLE further produced statistical models of wave activity for different types of waves based on the wave database. These models - or maps - provide statistical distribution of amplitudes and, moreover, wave normal angles and other polarization and propagation characteristics, which determine how the waves interact with particles.

  This coordinated, synergistic data processing and the development and public provision of the resulting databases have **added value to European space missions and earth-based observations by significantly contributing to the effective scientific exploitation of the data**. Moreover, MAARBLE has brought together European with Canadian and US research Groups who have not collaborated on a project before and has thus **enhanced the relations with established space powers thus adding value to European space missions**.

- The databases and the scientific results MAARBLE have already contributed to the optimal exploitation of the new space missions Swarm (of ESA) and Van Allen Probes (of NASA - formerly RBSP / Radiation Belt Storm Probes), and have thus **“contributed to the much needed coordination of the exploitation of ... future data collection”** (Swarm and RBSP were “future missions” at the time MAARBLE started).
- As originally planned, MAARBLE collaborated closely with and provided data to the SPACECAST project to help improve their radiation belt forecasts.
- MAARBLE attracted a number of young researchers into science, who benefited from working in distinguished research teams, producing world-class science.

- The MAARBLE project has published a large number of research papers in scientific peer reviewed journals that has increased our understanding of the basic physical processes controlling radiation belt dynamics.
- As MAARBLE project results have promoted the understanding of radiation belt variability, they have the potential of contributing to the protection of space-based infrastructure that is increasingly used for European security and defence.
- MAARBLE project results will also have a positive long-term impact on space exploration - one of the pillars of the European Space Policy - because radiation belt dynamics has direct impacts on spacecraft and on humans in space.

At this point we would like to include the final remarks we received from the members of the External Advisory Committee of the MAARBLE project:

Looking back upon the project from this vantage point, and summarizing the activities conducted to date, it is clear that the objectives of the project have been fully met.
The data sets produced by the MAARBLE team, and the scientific discussions held when preparing and delivering them, have led to the submission and publication of a series of excellent papers in leading journals within our research field.
Furthermore, the data sets contain the material for many more studies, that members of the team and those outside will be able to conduct in future, because the data products generated by the MAARBLE project have been deposited in the Cluster Science Archive - an open-access data archive, which aims at preserving the data on the long-term, together with the descriptive and documentary elements making it possible to select and interpret them.
The MAARBLE data sets represent a treasure trove for future research within Europe and beyond. Their addition in the CSA will find maximum utility in both independent studies and studies in which they are correlated with the Cluster mission. The comprehensive empirical and theoretical models for the radiation belts developed by the project will be of immense importance in guiding future mission design and planning.
In addition to the excellent papers in leading journals within our research field, the MAARBLE project results have been well-disseminated to interested users at the
European Geophysical Union's annual meeting (twice), at the American Geophysical Union's annual meeting and at the recent 'Geospace revisited' meeting organized by Professor Daglis. Furthermore, there has been also a very efficient public outreach campaign. The MAARBLE website has a dedicated public outreach section, which provides simplified science information on the project and on the geospace environment and its effects on humans and on spacecraft. A series of very successful public talks have been given on the occasion of the MAARBLE project meetings, and interviews of the project members appear on the web and in news media. And, most original of all, a "MAARBLE Sounds of Space" Musical Composition Contest was organised, combining scientific and artistic ways of thinking, were composers presented electroacoustic music based on natural sounds of the Earth’s magnetosphere.
As a final comment, we would like to note that the proposed work created a strong international team of scientists capable of working closely together and achieving their

common objectives. The team should investigate all possible ways of continuing their work together, and funding agencies should explore the possibility of continuing funding for this timely and cutting edge work on the radiation belts.

Iannis Dandouras, IRAP, France
David Sibeck, NASA/GSFC, USA
Eftyhia Zesta, NASA/GSFC, USA

5. Project website

Project website address: http://www.maarble.eu

Contact:
Prof. Dr. Ioannis A. Daglis
Department of Physics
University of Athens
Tel.: +30-210-7276857, +30-210-7276725, +30-210-7276715
email: iadaglis@phys.uoa.gr